Supplement of Atmos. Chem. Phys., 26, 3253–3276, 2026
https://doi.org/10.5194/acp-26-3253-2026-supplement

Supplement of

Atmospheric CO_2 dynamics in a coastal megacity: spatiotemporal patterns, sea–land breeze impacts, and anthropogenic–biogenic emission partitioning

Jinwen Zhang et al.

Correspondence to: Mei Li (limei@jnu.edu.cn)

In this document, we describe: (1) site selection strategy; (2) monitoring system and instrument principles; (3) wind fields; (4) background concentrations.

S1. Site selection strategy

The site selection process for Guangzhou's greenhouse gas monitoring network comprises preliminary screening, precise screening, and field surveys. The preliminary screening phase involves analyzing the city's dominant wind directions, topographic features, and emission distribution to establish a baseline understanding (Fig. S1). Drawing on experiences from other cities and considering local conditions and construction costs, the initial plan proposed three monitoring stations:

1. Urban station: located in the densely populated central urban area to monitor atmospheric CO_2 signals driven by anthropogenic emissions.
2. Coastal station: positioned in the southern coastal region to study the impacts of regional transport and coastal-specific weather systems (notably sea–land breeze) on CO_2 concentrations.
3. Suburban station: situated in the northern suburbs to capture CO_2 dynamics under urban ecosystem conditions.

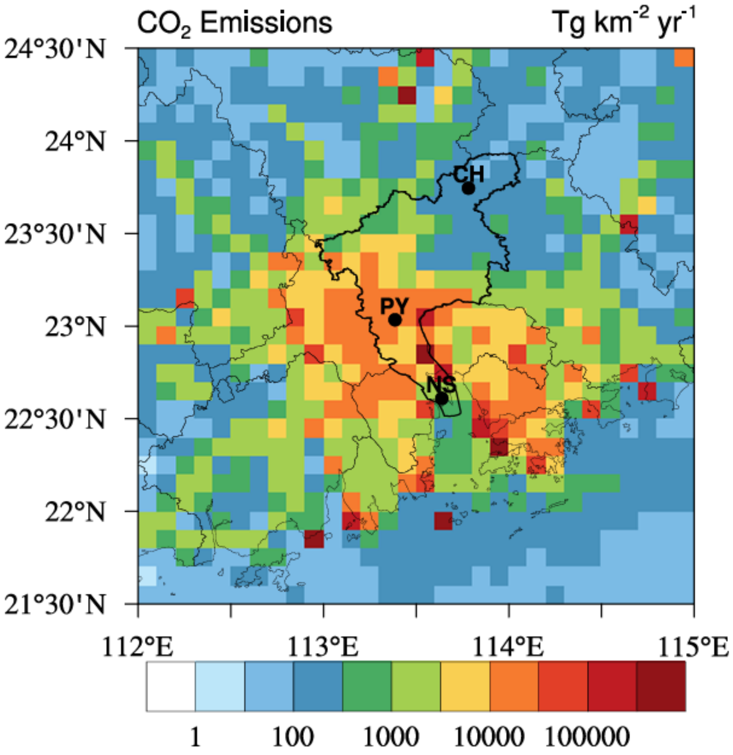

Figure S1. CO_2 emissions in Guangzhou and surrounding cities based on the Emissions Database for Global Atmospheric Research (EDGAR) Community GHG database (EDGAR_2024_GHG; 2023; 0.1° × 0.1°) (Crippa et al., 2024).

After determining the number of stations, satellite remote sensing was used to identify high-, medium-, and low-CO_2 concentration zones. A cluster analysis model screened 5–10 times the proposed number of candidate sites. These candidates were further evaluated using the WRF-STILT model to analyze their sensitivity to CO_2 footprints, ensuring representative and sensitive site selection. Field surveys for final site selection included the following criteria:

(1) Emission sources: greenhouse gas emission sources within a 1 km radius should be maintained at minimal levels.

(2) Sampling accessibility: a 360° horizontal capture space around the sampling inlet.

(3) Geological stability: long-term geological stability to avoid impacts from floods, wildfires, or landslides.

(4) Infrastructure: minimal electromagnetic interference, stable power supply, lightning protection, and accessible communication lines.

(5) Mobile monitoring: at least one week of mobile greenhouse gas monitoring at each candidate site.

Priority was given to newly constructed towers or existing open high towers for sampling, as these structures minimize airflow disturbances from supporting frameworks (Verhulst et al., 2017). Towers exceeding 50 m in height were preferred; however, such platforms account for less than 1 % in Guangzhou and are often located in inaccessible areas. Thus, sites near 50 m were prioritized to ensure well-mixed air sampling and avoid local anthropogenic or natural source–sink influences.

S2. Monitoring system

At the inlet front end, hydrophobic PTFE capsule filters and stainless steel tube clamps are installed. The capsule filters remove solid particles larger than 10 μm. Ambient air samples are drawn through 10 mm diameter PTFE-coated black aluminum-plastic tubes via a vacuum pump, with a maximum flow rate of 2 L min^{-1}. Additional filters in the tubing system remove solid particles larger than 2 μm and liquid droplets larger than 0.03 mm. The gas passes through a primary dehumidifier to reduce the dew point temperature to 2–10 °C, preventing condensation in the intake pipes. An ultra-low-temperature automatic cryogenic trap and a multi-channel gas intake system are also installed. Using built-in compressor cooling, the aluminum alloy cryogenic trap can lower the dew point temperature to −50 °C. Optimization of the control program minimizes maintenance requirements for the condensation dehumidifier, ensuring optimal system performance and reducing data artifacts during gas channel switching. Before entering the analyzers, samples pass through the calibration module, where periodic calibration curve establishment and target gas verification ensure measurement precision, accuracy, and long-term stability (detailed in Section 2.3).

The Picarro G2401 greenhouse gas analyzer employs Cavity Ring-Down Spectroscopy (CRDS). Its working principle is based on the near-infrared absorption spectrum unique to greenhouse gases like CO_2. When an infrared laser is reflected by high-reflectivity mirrors within the measurement cavity, the light intensity decays exponentially. The gas concentration is determined by calculating the difference in ring-down time between an empty cavity and one filled with the target gas. The ABB GLA331-GGA greenhouse gas analyzer utilizes Off-Axis Integrated Cavity Output Spectroscopy (OA-ICOS). This technology creates an optical cavity using two highly reflective mirrors, enabling the laser to undergo multiple reflections between them. This amplifies the absorption signal, enhancing measurement sensitivity.

S3. Wind fields

Wind speed and direction are critical indicators of temporal variations in atmospheric CO_2 concentrations. Figure S2 presents seasonal wind frequency monitoring results for the NS and PY stations, with wind speed resolution of 1.5 m s^{-1} and directional resolution of 10°:

(1) NS Station: average wind speed = 2.86 m s^{-1}. Dominant southerly winds in spring/summer (64 % and 57 % frequency) and northerly winds in autumn/winter (66 % and 56 %).

(2) PY Station: average wind speed = 2.12 m s^{-1}. Prevailing northeastern and southeastern winds across seasons.

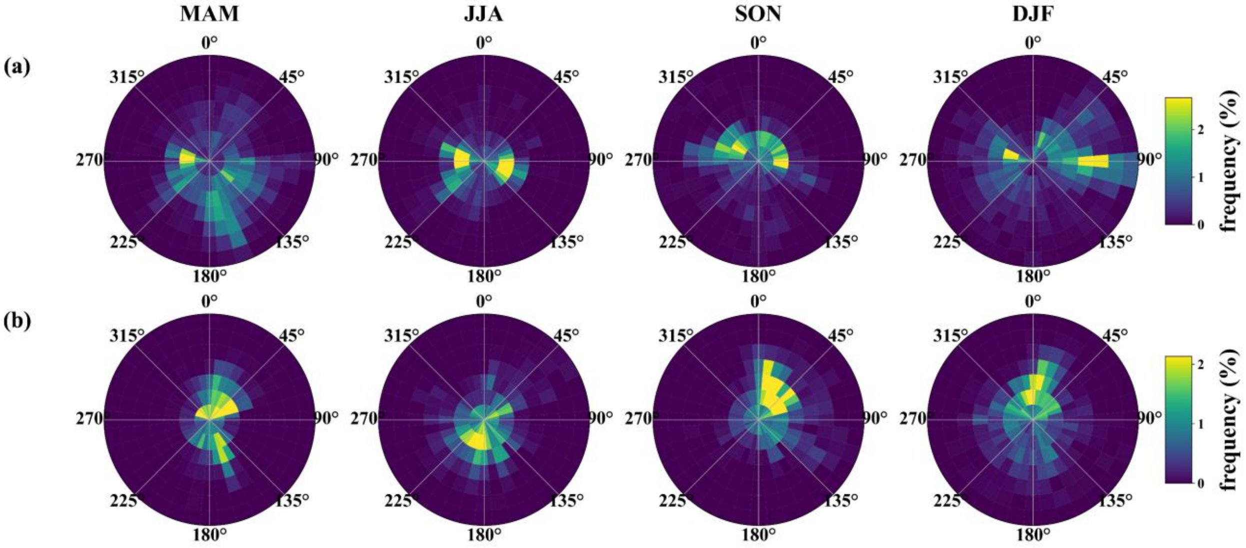

Figure S2. Observed wind frequency as a function of wind speed and wind direction in spring (MAM), summer (JJA), autumn (SON), and winter (DJF) at **(a)** NS and **(b)** PY from January 2023 to September 2024.

S4. Background concentrations

Real-time monitoring of atmospheric background values entirely unaffected by local sources and sinks in urban areas is challenging. Due to technical and logistical constraints such as site accessibility and power supply, very few monitoring stations are sufficiently remote to remain permanently exposed to pristine air masses (Fang et al., 2015). With urbanization, many regional background stations in suburban areas are increasingly influenced by urban carbon sources, leading to overestimated urban background values (Chen et al., 2024). Here, urban background concentrations are defined as representative values of air masses entering the city from upwind directions, unaffected by local sources or sinks (Verhulst et al., 2017; Mitchell et al., 2018).

This study combines dominant urban wind patterns, atmospheric transport models, NOAA Earth System Research Laboratory/Global Monitoring Laboratory (NOAA GML) background stations, and Carbon Tracker assimilation data to determine atmospheric CO_2 and CO background values for Guangzhou. Seasonal dominant wind directions at urban stations exhibited similar characteristics (Fig. S2), prompting a focus on summer and winter for airmass origin analysis. Figure S3 illustrates the spatial distribution of average afternoon (12:00–16:00 LT) atmospheric footprints during summer (July) and winter (December) over Guangzhou. Summer footprints primarily spanned southern urban and marine regions, while winter footprints extended to northeastern and southeastern urban and marine areas. By tracking air particles entering the city and using samples from the CO_2 GLOBALVIEWplus v10.1 ObsPack (Schuldt et al., 2024), two NOAA GML background stations—Hok Tsui (HKG) and Dongsha Island (DSI)—were identified as potential marine background references for Guangzhou. Air particles from upwind directions passed through both stations in all seasons.

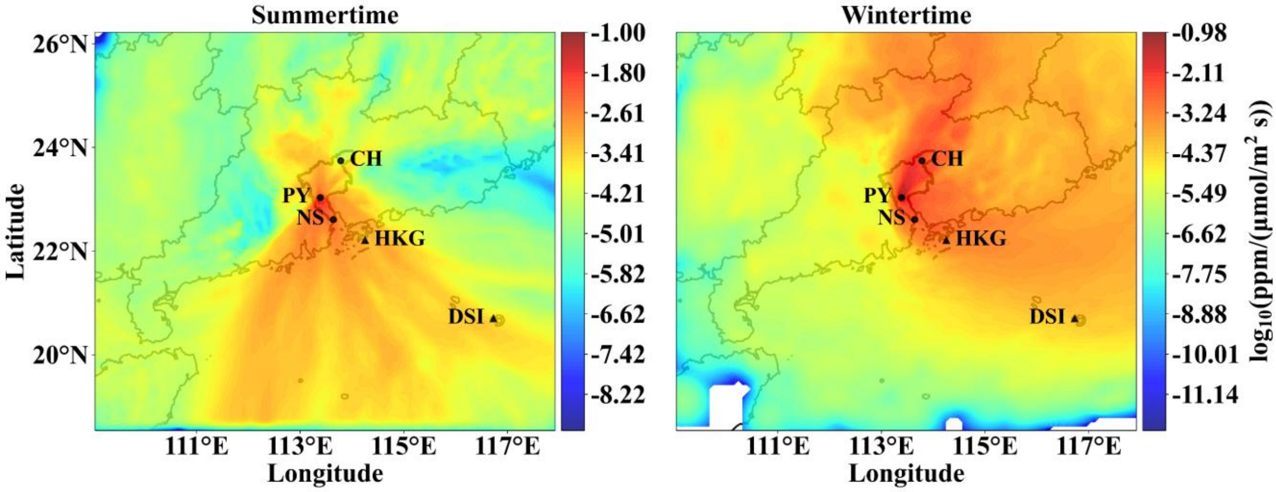

Figure S3. Spatial distribution of average atmospheric footprints during afternoon hours (12:00–16:00 LT) in summer (July) and winter (December) based on the PY station.

We compared decadal CO_2 time series from these stations (Fig. S4) and applied CCGCRV curve-fitting software for smoothing (Thoning et al., 1989). HKG data showed significant deviations from smoothed trends, suggesting contamination by local CO_2 surface fluxes. In contrast, DSI data consistently fell within HKG's range, indicating its suitability as Guangzhou's marine background. For further validation, we compared concentration values from NOAA's CarbonTracker (version CT-NRT.v2024-5) at grid cells where air particles last resided with DSI observations (Jacobson et al., 2024). During 2023, residuals between smoothed values were < 2 ppm, with a mean residual of 0.81 ± 0.85 ppm (Fig. S5), confirming DSI's reliability. Due to DSI's sparse weekly flask sampling, Carbon Tracker data were adopted for marine CO_2 background concentrations. For CO, lacking Carbon Tracker data, smoothed DSI CO observations served as the urban background reference.

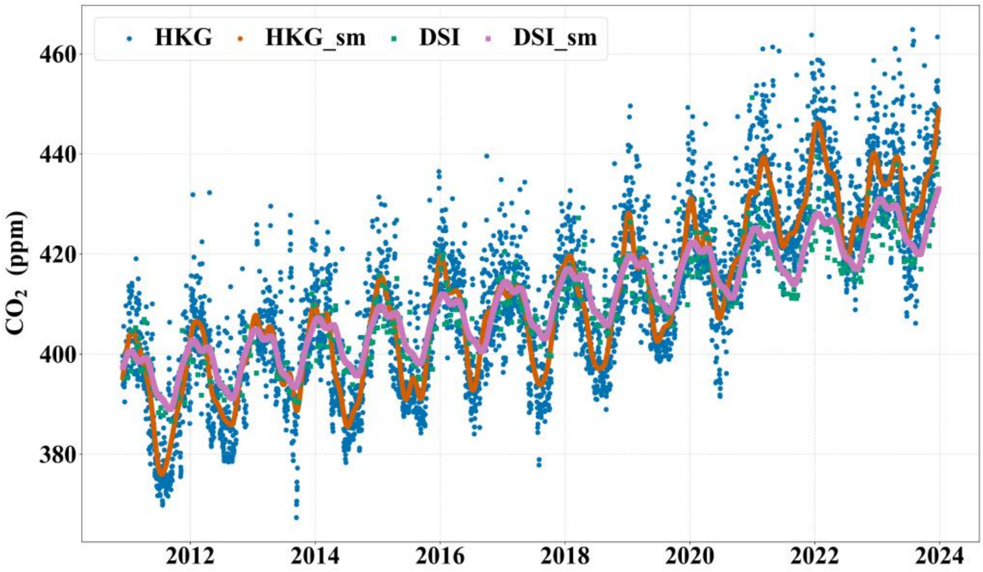

Figure S4. Time series of atmospheric CO$_2$ concentrations showing both raw monitored data and smoothed values at HKG and DSI stations from November 2, 2010, to December 31, 2023.

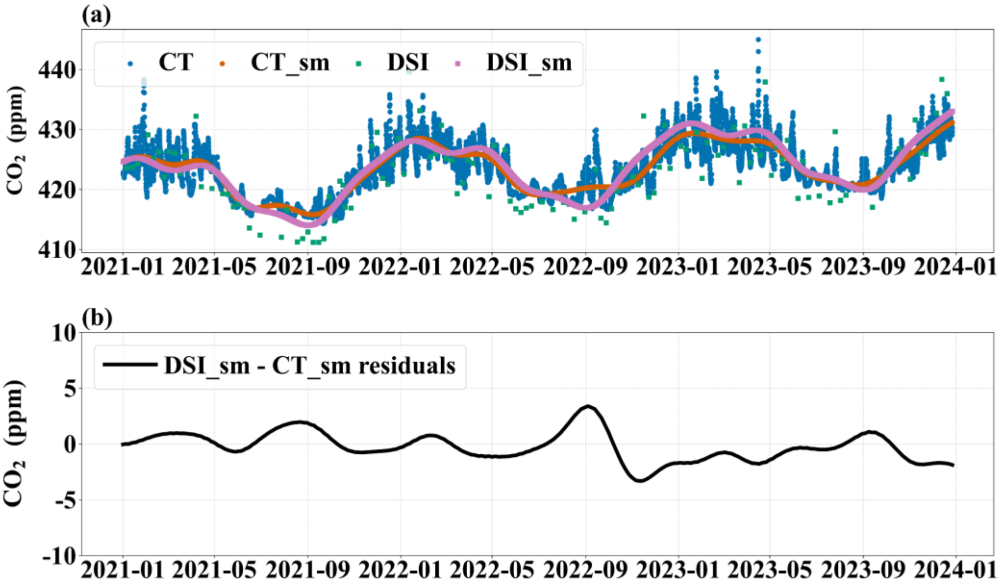

Figure S5. (a) Time series of atmospheric CO$_2$ concentrations showing both raw monitored/simulated data and smoothed values for DSI and CarbonTracker from January 1, 2021, to December 26, 2023. **(b)** Residuals between DSI and CarbonTracker smoothed values.

Table S1. Summary of sea–land breeze day (SLBD) identification methods

Study area	**Data**	**SLBD identification criteria**	**References**
Pearl River Estuary	Observational data	Nighttime offshore winds or calm; ≥ 4 consecutive daytime onshore winds; ΔP ≤ 5 hPa; land–sea ΔT > 3 °C	(Qiu and Fan, 2013)
Tianjin	Observational data	≤ 1 isobar line on surface weather maps; land–sea ΔT > 0 °C; ≥ 3 consecutive onshore/offshore winds from sunrise to 2 h post-sunset	(Hao et al., 2017)
West African Coast	Reanalysis & observational data	Offshore/calm winds 6 h before sunrise and 2 h after sunrise; ≥ 2 consecutive onshore winds post-sunrise; ΔT > 0 °C; ≥ 4 h daily sunlight	(Coulibaly et al., 2021)
Zhuhai	Observational data	24 h average wind speed < 10 m s^{-1}; ≥ 3 occurrences of land/sea breeze; absolute wind direction difference between 02:00 and 14:00 = 90–270°	(Zhang et al., 2024)
Pearl River Estuary	Observational data	≤ 1 isobar line at 08:00 and 20:00; ≥ 4 consecutive land/sea breeze hours or ≥ 4 occurrences within 5 consecutive hours; no precipitation 3 h before/after SLB transition	(Mai et al., 2024)
Coastal China	Reanalysis & observational data	24 h average wind speed < 10 m s^{-1}; ≥ 4 consecutive land/sea breeze hours; alternating sea–land breeze cycles within 24 h	(Huang et al., 2025)

Table S2. Summary of 2023 tropical cyclones (TCs) and impact windows in the Pearl River Delta (PRD)

TC number	International name	Impact start	Impact end	PRD / Guangzhou impacts (summary)	References
2304	Talim	2023-07-15	2023-07-18	Gusty winds and storm surge along the western PRD; strong winds and squally showers in Guangzhou on Jul 17.	2023 Guangdong–Hong Kong–Macao Greater Bay Area (GBA) Climate Monitoring Bulletin (https://my.weather.gov.hk/en/wxinfo/pastwx/2023/files/GD_HK_Mac_GBA_2023.pdf)
2305	Doksuri	2023-07-24	2023-07-29	Peripheral rainbands and thunderstorms; local advisories issued in PRD/Guangzhou.	
2309	Saola	2023-09-01	2023-09-03	Severe gales and heavy rain across PRD; service suspensions; multiple warnings in Guangzhou and surrounding cities.	
2311	Haikui	2023-09-05	2023-09-11	Remnant low brought prolonged heavy rain in PRD; locally record-breaking September rainfall in parts of Guangdong.	
2314	Koinu	2023-10-05	2023-10-09	Sustained gales and heavy rain in PRD; transport/service disruptions; multiple warnings in Guangzhou.	
2316	Sanba	2023-10-19	2023-10-20	Peripheral effects in PRD with rain/gusts; main impacts over western Guangdong (Zhanjiang/Maoming) and Hainan.	

Table S3. Seasonal temperature averages (°C) at each station

Station	**Season**	**20:00–05:00**	**09:00–18:00**	**0:00–23:00**
CH[*]	autumn	22.49	26.12	23.95
	spring	20.76	23.36	21.84
	summer	26.39	29.77	27.80
	winter	13.04	16.07	14.26
PY	autumn	26.21	28.70	27.19
	spring	23.34	25.41	24.18
	summer	29.19	31.67	30.21
	winter	16.63	18.61	17.38
NS	autumn	26.40	29.32	27.57
	spring	23.43	25.10	24.10
	summer	29.21	31.32	30.10
	winter	17.37	18.85	17.91

***** CH station's temperature measurements were collected from an atmospheric monitoring station 1 km away.

Table S4. Marine background concentration uncertainties

	Uncertainty estimates	**Summer**	**Winter**
CO_2 (ppm)	$CT_{co2,r}$	0.46	0.45
	$CT_{co2,s}$	0.84	0.54
	$BG_{u,co2}$	0.96	0.70
CO (ppb)	$OBS_{co,r}$	2.10	11.79
	$OBS_{co,s}$	12.50	14.08
	$BG_{u,co}$	12.68	18.36

Table S5. July–December contrasts in daily afternoon means (PY, 12:00–16:00 LT).
(Δ = winter − summer; units: μmol m^{-2} s^{-1})

Component	July Mean ± SE	Dec Mean ± SE	July → Dec (median, IQR)	Δ (Welch 95 % CI)	Welch p	Mann–Whitney p	Bootstrap 95 % CI of Δ
CO_2tot	2.38 ± 0.45	13.50 ± 2.20	2.00 (0.72–3.05) → 10.34 (7.16–15.00)	+11.12 [6.40, 15.83]	9.83×10^{-5}	4.06×10^{-7}	[7.10, 15.67]
CO_2ff	5.97 ± 0.75	13.56 ± 2.40	4.33 (3.58–7.81) → 10.70 (6.74–18.28)	+7.59 [2.36, 12.82]	0.0066	0.002	[3.09, 12.65]
CO_2bio	−3.59 ± 0.63	−0.06 ± 1.13	−3.17 (−5.42–−1.39) → −0.20 (−2.11–2.59)	+3.53 [0.87, 6.19]	0.011	0.003	[1.01, 6.04]

Table S6. Wintertime (12:00–16:00 LT) paired-day sensitivity of PY inferred fluxes to STILT parameter choices (n = 18). Variants (particle number, grid spacing, backward duration) are compared with the baseline (500 particles, 0.08°, 72 h). Metrics report effect size (pct_diff_% and 95 % CI), day-to-day consistency (Pearson r), RMSE (μmol m^{-2} s^{-1}), and detectability (paired t-test p value). Upper block: CO_2ff; lower block: CO_2tot. Across the baseline plus six variants, the day-by-day ensemble spread—computed as the standard deviation across the seven runs for each day and then summarized by the median—was 0.20–0.21 μmol m^{-2} s^{-1} (median CV ≈ 1.8 %).

Metric	Comparison	Pct_diff_%	Pearson_r	RMSE	P_value	CI95_lo	CI95_hi
PY_CO_2ff	Back 120 h vs Base (72 h)	−1.05	0.9994	0.38	0.1136	−0.3216	0.0376
	Back 96 h vs Base (72 h)	−1.34	0.9993	0.45	0.0831	−0.3904	0.0265
	Particles 1000 vs Base (500)	−0.56	0.9996	0.33	0.3410	−0.2380	0.0871
	Particles 2000 vs Base (500)	−0.24	0.9995	0.31	0.6738	−0.1916	0.1269
	Res 0.05° vs Base (0.08°)	−0.72	0.9996	0.31	0.1917	−0.2506	0.0542
	Res 0.10° vs Base (0.08°)	−1.47	0.9997	0.39	0.0269	−0.3729	−0.0257
PY_CO_2tot	Back 120 h vs Base (72 h)	−1.31	0.9992	0.44	0.0862	−0.3819	0.0280
	Back 96 h vs Base (72 h)	−1.33	0.9992	0.45	0.0916	−0.3900	0.0322
	Particles 1000 vs Base (500)	−0.52	0.9996	0.28	0.2983	−0.2098	0.0683
	Particles 2000 vs Base (500)	−0.31	0.9995	0.29	0.5502	−0.1864	0.1029
	Res 0.05° vs Base (0.08°)	−0.78	0.9996	0.31	0.1527	−0.2541	0.0431
	Res 0.10° vs Base (0.08°)	−1.40	0.9997	0.35	0.0164	−0.3394	−0.0393

Table S7. Wintertime (12:00–16:00 LT) paired-day sensitivity of PY CO_2bio inferred fluxes to STILT parameter choices (n = 18). Variants (particle number, grid spacing, backward duration) are compared with the baseline (500 particles, 0.08°, 72 h). We report the absolute paired-day test–baseline difference, defined as ΔCO_2bio = CO_2bio (variant) − CO_2bio (baseline), summarized by the paired-day mean (Δ; $\mu mol\ m^{-2}\ s^{-1}$) and its 95 % confidence interval (CI95_lo, CI95_hi; $\mu mol\ m^{-2}\ s^{-1}$). Because wintertime CO_2bio at PY is close to zero, percent differences are not shown. Across-run daily spread of CO_2bio—defined as the day-by-day standard deviation across the baseline and all variants—has median 0.045 and IQR 0.016–0.067 $\mu mol\ m^{-2}\ s^{-1}$.

Metric	**Comparison**	**Mean (ΔCO_2bio)**	**CI95_lo**	**CI95_hi**
PY_CO_2bio	Back 120 h vs Base (72 h)	−0.035	−0.094	0.024
	Back 96 h vs Base (72 h)	0.003	−0.057	0.063
	Particles 1000 vs Base (500)	0.005	−0.031	0.041
	Particles 2000 vs Base (500)	−0.009	−0.052	0.033
	Res 0.05° vs Base (0.08°)	−0.007	−0.047	0.033
	Res 0.10° vs Base (0.08°)	0.010	−0.043	0.063

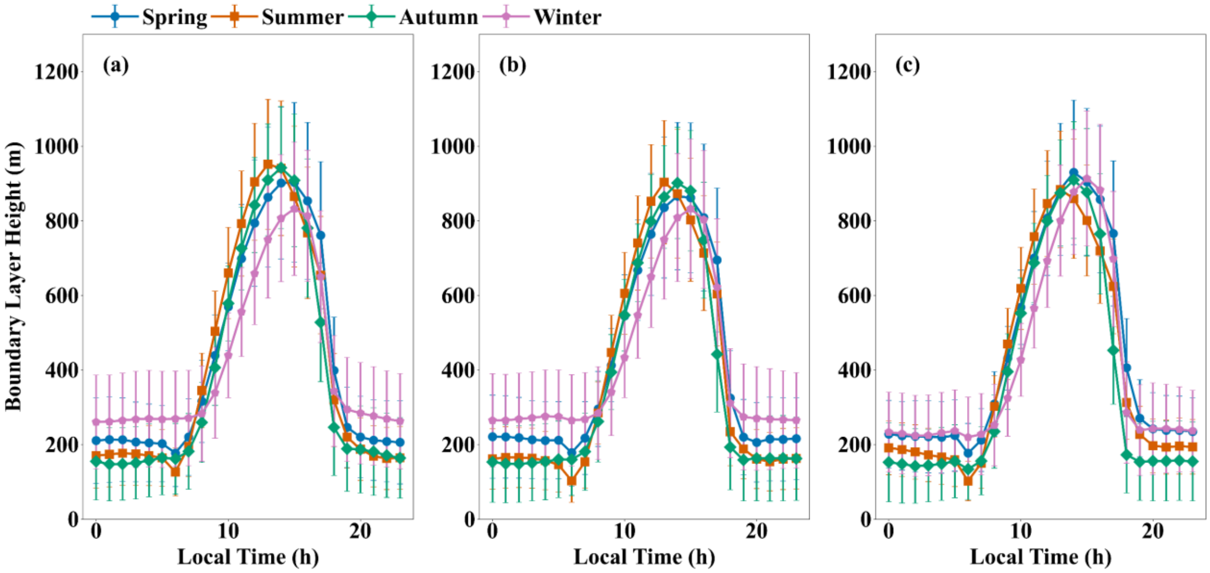

Figure S6. Diurnal variations in atmospheric boundary layer height at the **(a)** NS, **(b)** PY, and **(c)** CH stations across seasons. The planetary boundary layer height data were obtained from the ERA5 reanalysis product with a spatial resolution of 0.25° × 0.25° (Hersbach, 2023). Error bars indicate ± 1 standard deviation (SD).

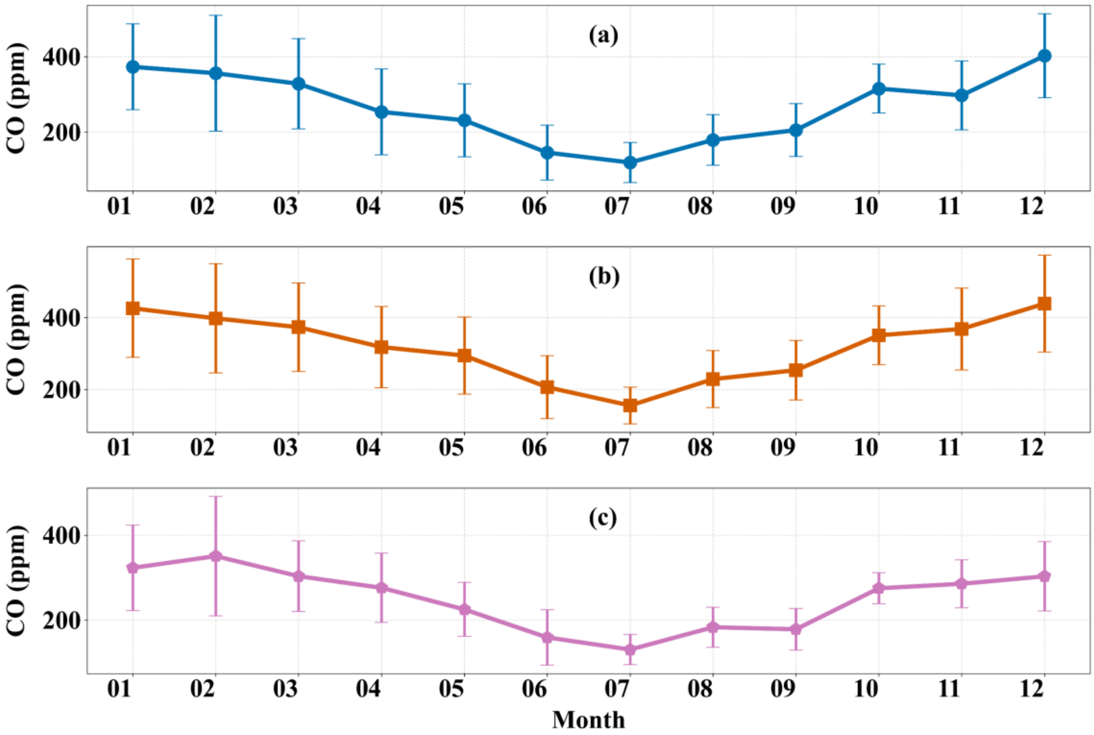

Figure S7. Monthly mean CO concentrations at the **(a)** NS, **(b)** PY, and **(c)** CH stations. Error bars indicate ± 1 SD.

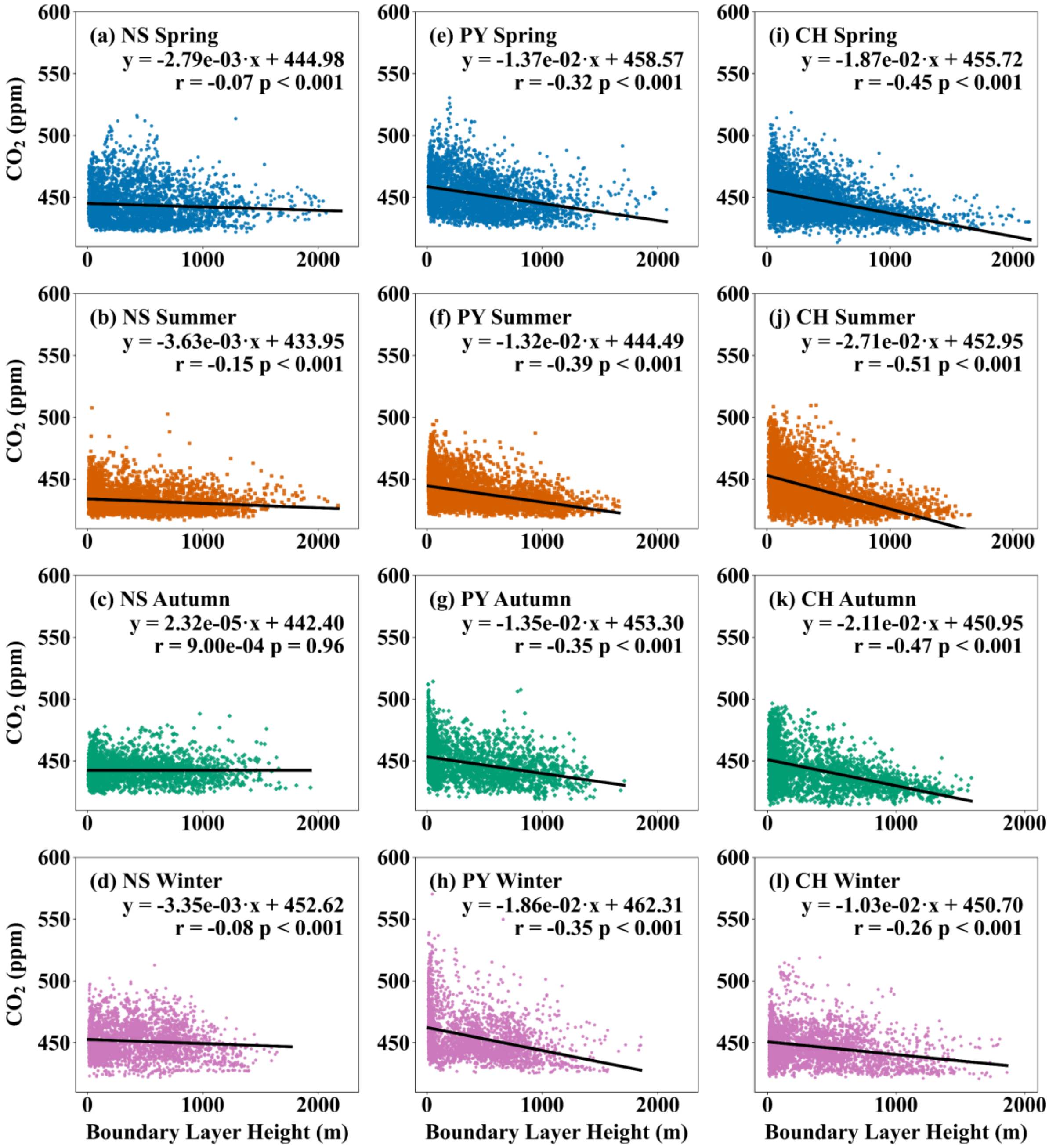

Figure S8. Correlations between atmospheric CO_2 concentrations and boundary layer height at the **(a–d)** NS, **(e–h)** PY, and **(i–l)** CH stations across seasons.

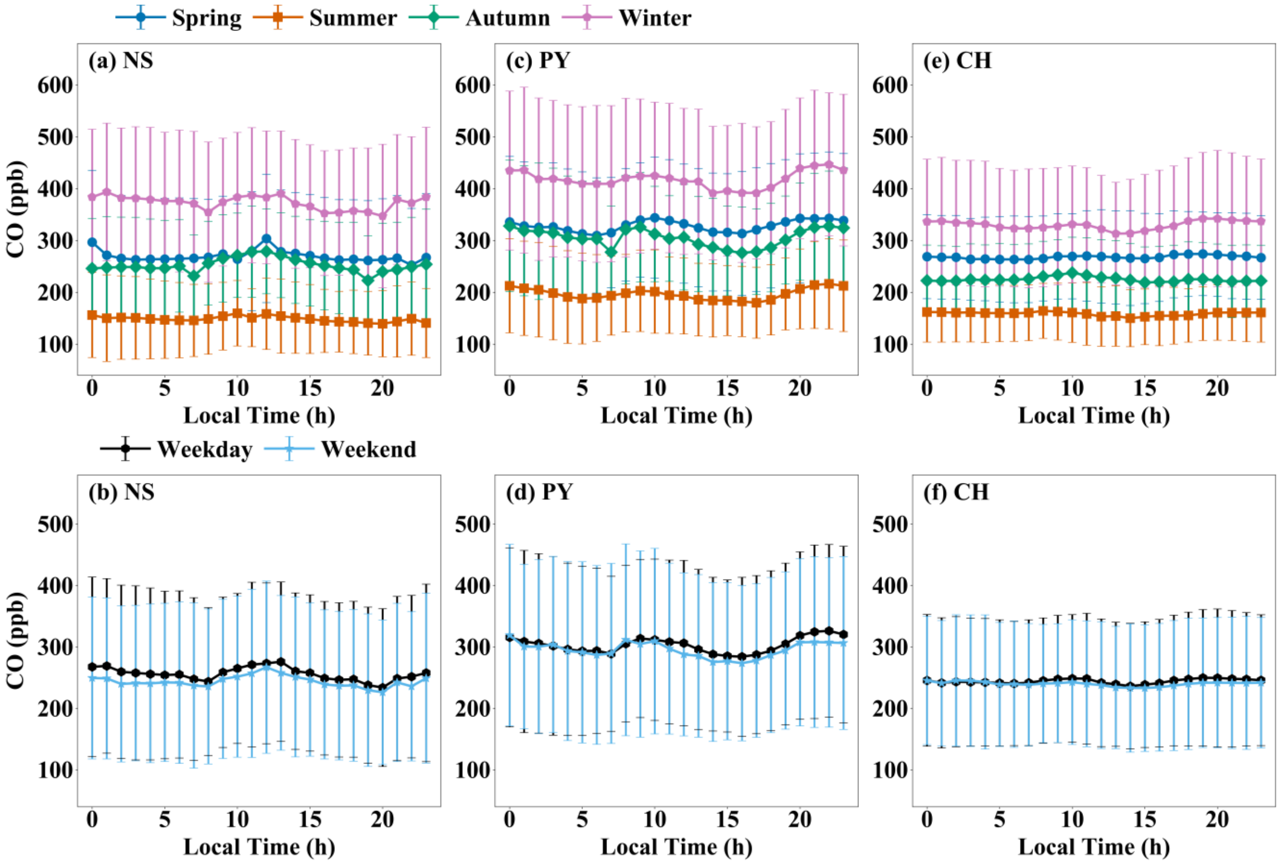

Figure S9. Diurnal CO_2 variations at the **(a–b)** NS, **(c–d)** PY, and **(e–f)** CH stations, shown across seasons (upper panels) and weekdays/weekends (lower panels). Seasons are defined as spring (Mar–May), summer (Jun–Aug), autumn (Sep–Nov), and winter (Dec–Feb). Error bars indicate ± 1 SD.

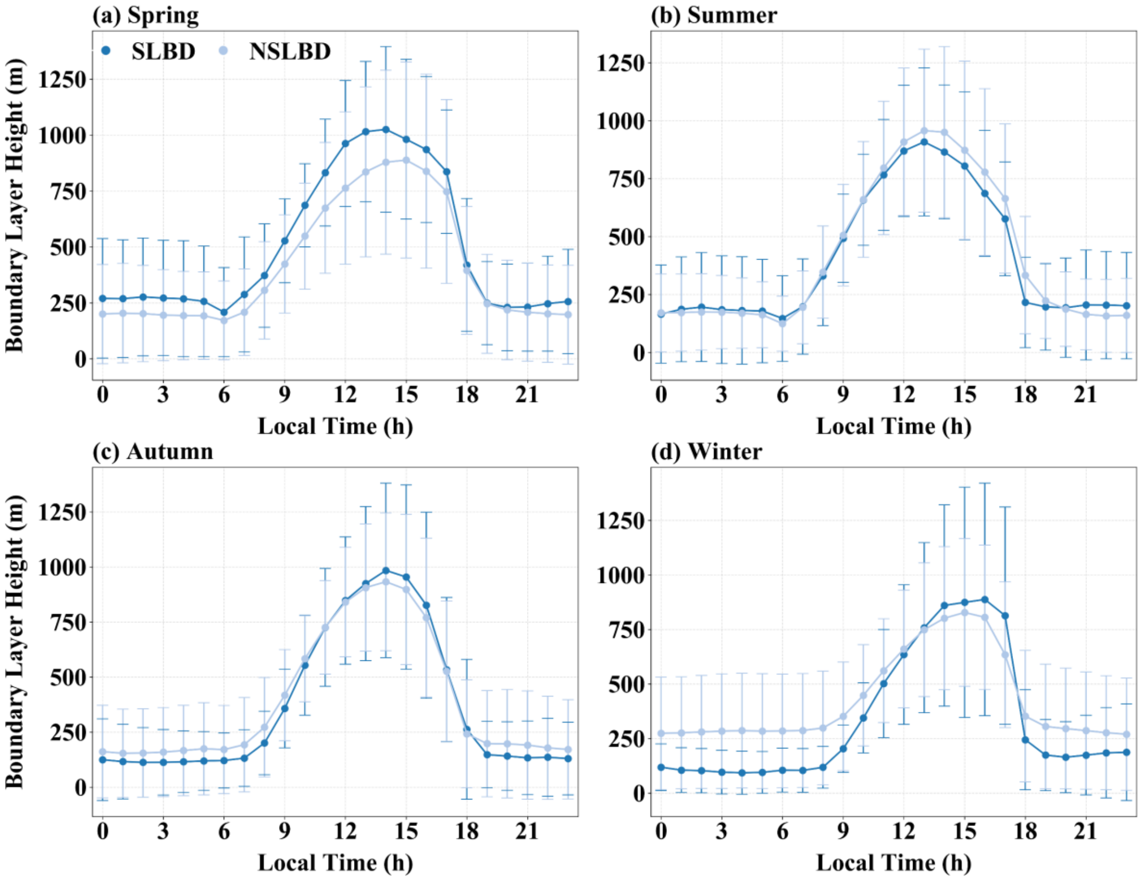

Figure S10. Diurnal variations in atmospheric boundary layer height at the NS station during sea–land breeze days (SLBD) and non-SLB days (NSLBD) for **(a)** spring (Mar–May), **(b)** summer (Jun–Aug), **(c)** autumn (Sep–Nov), and **(d)** winter (Dec–Feb). Error bars indicate ± 1 SD.

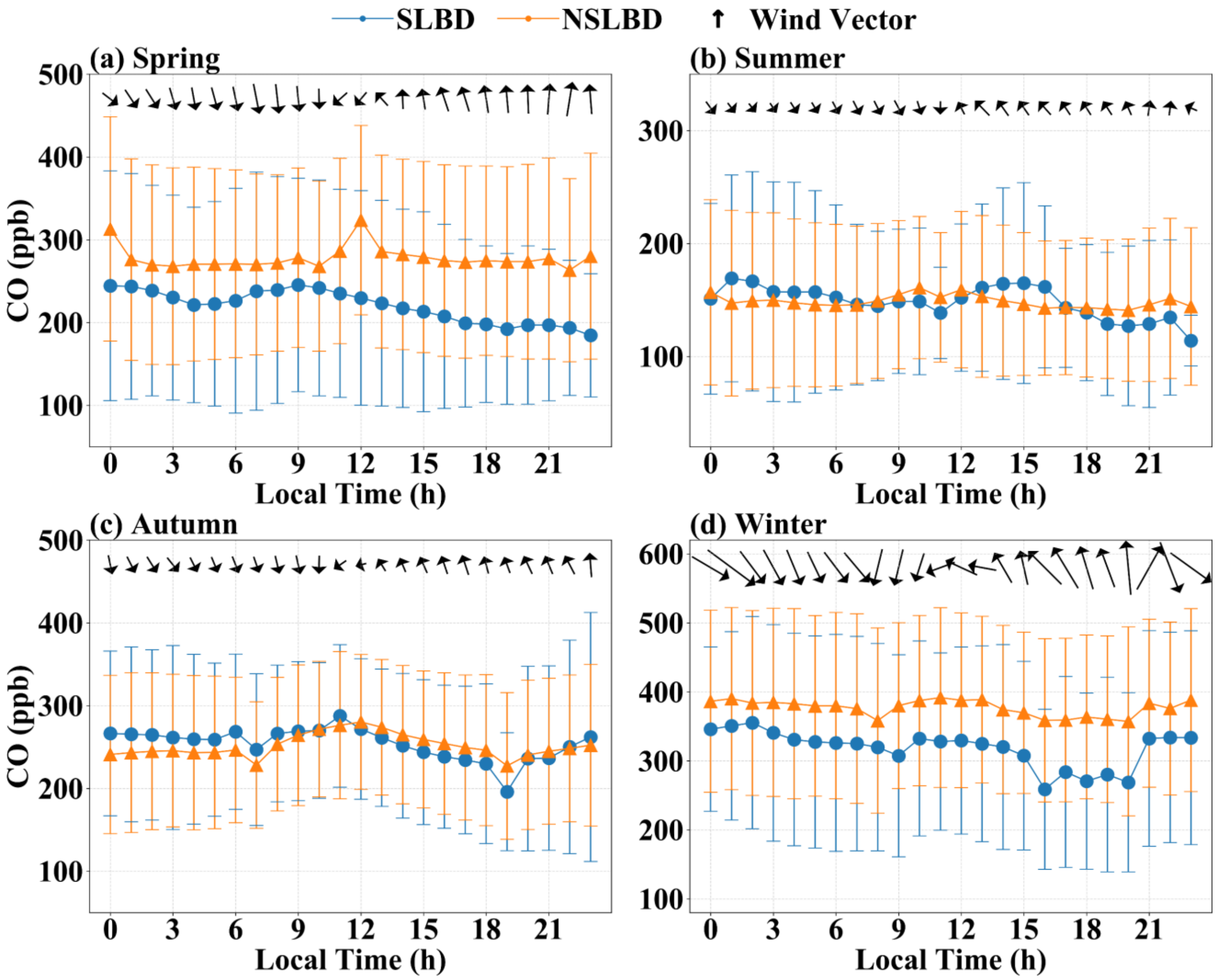

Figure S11. Diurnal variations in CO concentrations, wind direction, and wind speed at the coastal station (NS) during sea–land breeze days (SLBD) and non-SLB days (NSLBD) for **(a)** spring (Mar–May), **(b)** summer (Jun–Aug), **(c)** autumn (Sep–Nov), and **(d)** winter (Dec–Feb). Error bars indicate ± 1 SD.

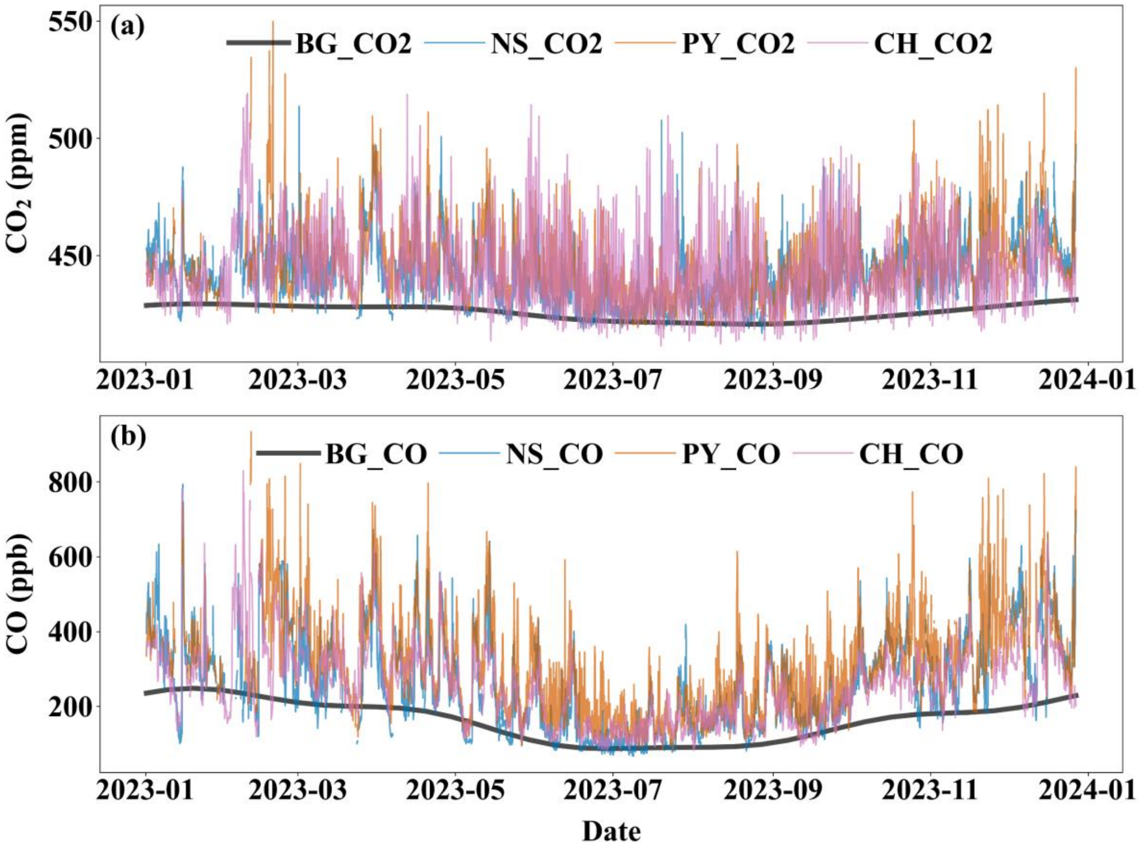

Figure S12. Time series of **(a)** CO_2 and **(b)** CO concentrations at each station compared with urban background levels.

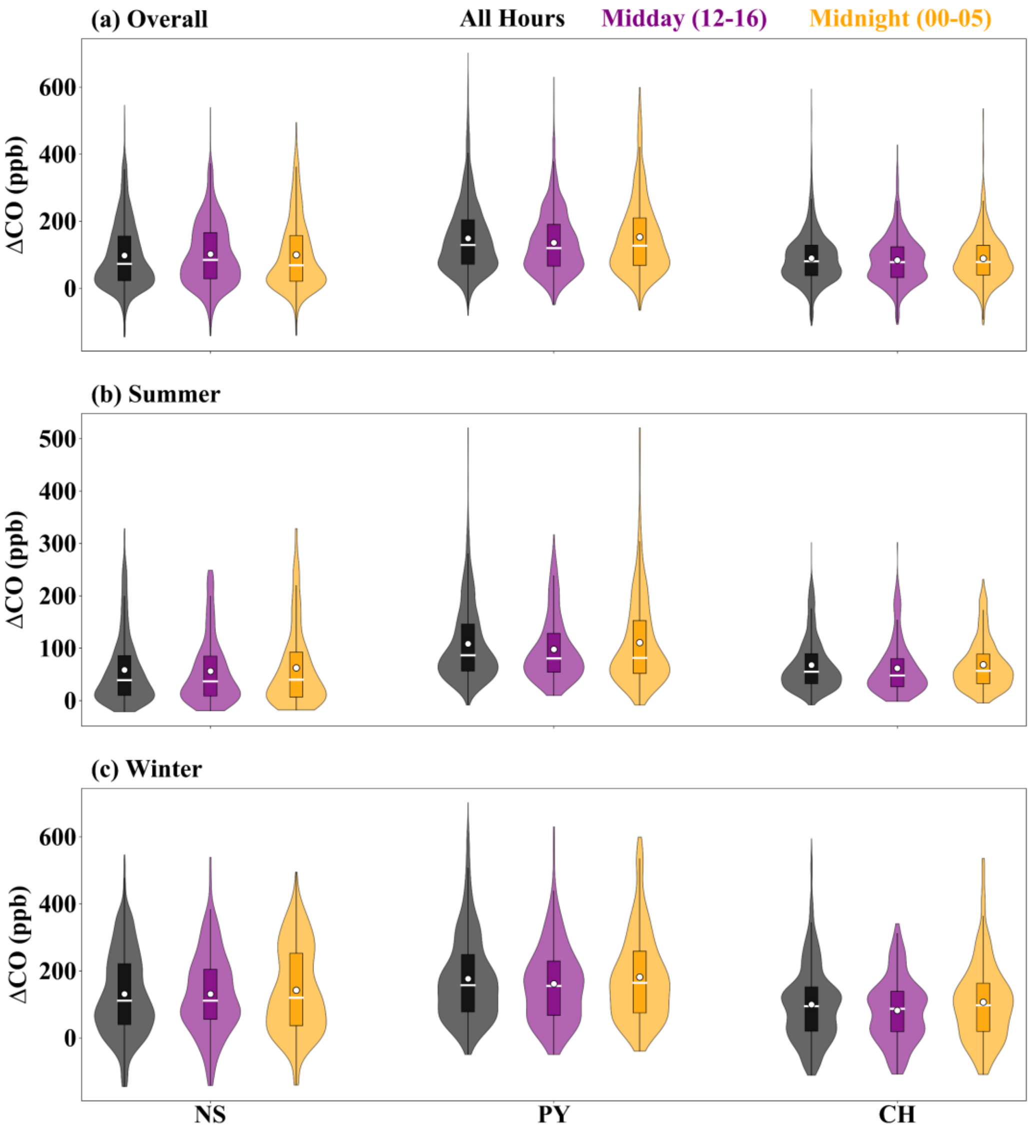

Figure S13. Distributions of hourly CO enhancement (ΔCO) above the background concentrations at NS, PY, and CH during the **(a)** overall, **(b)** summer, and **(c)** winter periods, shown for all hours, midday (12:00–16:00 LT), and midnight (00:00–05:00 LT). White dots denote the mean values, and white horizontal lines denote the median values.

References

Chen, Y., Lu, Y., Qi, B., Ma, Q., Zang, K., Lin, Y., Liu, S., Pan, F., Li, S., and Guo, P.: Atmospheric CO_2 in the megacity Hangzhou, China: Urban-suburban differences, sources and impact factors, Sci. Total Environ., 926, 171635, https://doi.org/10.1016/j.scitotenv.2024.171635, 2024.

Coulibaly, A., Omotosho, B. J., Sylla, M. B., Diallo, Y., and Ballo, A.: Numerical simulation of land and sea-breeze (LSB) circulation along the Guinean Coast of West Africa, Model. Earth Syst. Environ., 7, 2031-2045, https://doi.org/10.1007/s40808-020-00953-0, 2021.

Crippa, M., Guizzardi, D., Pagani, F., Banja, M., Muntean, M., Schaaf, E., Monforti-Ferrario, F., Becker, W. E., Quadrelli, R., Risquez Martin, A., Taghavi-Moharamli, P., Köykkä, J., Grassi, G., Rossi, S., Melo, J., Oom, D., Branco, A., San-Miguel, J., Manca, G., Pisoni, E., Vignati, E., and Pekar, F.: GHG emissions of all world countries, Publications Office of the European Union, https://doi.org/10.2760/4002897, 2024.

Fang, S., Tans, P., Steinbacher, M., Zhou, L., and Luan, T.: Comparison of the regional CO_2 mole fraction filtering approaches at a WMO/GAW regional station in China, Atmos. Meas. Tech., 8, 5301-5313, https://doi.org/10.5194/amt-8-5301-2015, 2015.

Hao, T., Chen, S., Cai, Z., Shan, X., Meng, L., Han, S., and Dong, G.: Influence of sea breeze on atmospheric pollutant concentration over Tianjin, China Environmental Science, 37(9), 3247-3257, https://doi.org/10.3969/j.issn.1000-6923.2017.09.006, 2017.

Hersbach, H., Bell, B., Berrisford, P., Biavati, G., Horányi, A., Muñoz Sabater, J., Nicolas, J., Peubey, C., Radu, R., Rozum, I., Schepers, D., Simmons, A., Soci, C., Dee, D., Thépaut, J-N: ERA5 hourly data on single levels from 1940 to present, Copernicus Climate Change Service (C3S) Climate Data Store (CDS) [dataset], https://doi.org/10.24381/cds.adbb2d47, 2023.

Huang, Y., Li, S., Zhu, Y., Liu, Y., Hong, Y., Chen, X., Deng, W., Xi, X., Lu, X., and Fan, Q.: Increasing sea-land breeze frequencies over coastal areas of China in the past five decades, Geophys. Res. Lett., 52, e2024GL112480, https://doi.org/10.1029/2024GL112480, 2025.

Jacobson, A. R., Schuldt, K. N., Andrews, A., Miller, J. B., Oda, T., Basu, S., Mund, J., Weir, B., Ott, L., Aalto, T., Abshire, J. B., Aikin, K., Allen, G., Andrade, M., Apadula, F., Arnold, S., Baier, B., Bakwin, P., Bartyzel, J., Bentz, G., Bergamaschi, P., Beyersdorf, A., Biermann, T., Biraud, S. C., Blanc, P.-E., Boenisch, H., Bowling, D., Brailsford, G., Brand, W. A., Brunner, D., Bui, T. P., Burban, B., Bäni, L., Calzolari, F., Chang, C. S., Chen, H., Chen, G., Chmura, L., Clark, S., Climadat, S., Colomb, A., Commane, R., Condori, L., Conen, F., Conil, S., Couret, C., Cristofanelli, P., Cuevas, E., Curcoll, R., Daube, B., Davis, K. J., De Mazière, M., De Wekker, S., Dean-Day, J. M., Della Coletta, J., Delmotte, M., Di Iorio, T., DiGangi, E., DiGangi, J. P., Dickerson, R., Elsasser, M., Emmenegger, L., Fang, S., Forster, G., France, J., Frumau, A., Fuente-Lastra, M., Galkowski, M., Gatti, L. V., Gehrlein, T., Gerbig, C., Gheusi, F., Gloor, E., Goto, D., Griffis, T., Hammer, S., Hanisco, T. F., Hanson, C., Haszpra, L., Hatakka, J., Heimann, M., Heliasz, M., Heltai, D., Henne, S., Hensen, A., Hermans, C., Hermansen, O., Hintsa, E., Hoheisel, A., Holst, J., Iraci, L. T., Ivakhov, V., Jaffe, D. A., Jordan, A., Joubert, W., Kang, H.-Y., Karion, A., Kawa, S. R., Kazan, V., Keeling, R. F., Keronen, P., Kim, J., Klausen, J., Kneuer, T., Ko, M.-Y., Kolari, P., Kominkova, K., Kort, E., Kozlova, E., Krummel, P. B., Kubistin, D., Kulawik, S. S., Kumps, N., Labuschagne, C., Lam, D. H., Lan, X., Langenfelds, R. L., Lanza, A., Laurent, O., Laurila, T., Lauvaux, T., Lavric, J., Law, B. E., Lee, C.-H., Lee, J., Lehner, I., Lehtinen, K., Leppert, R., Leskinen, A., Leuenberger, M., Leung, W. H., Levin, I., Levula, J., Lin, J., Lindauer, M., Lindroth, A., Loh, Z. M., Lopez, M., Lunder, C. R., Löfvenius, M. O., Machida, T., Mammarella, I., Manca, G., Manning, A., Manning, A., Marek, M. V., Marklund, P., Marrero, J. E., Martin, M. Y., Martin, D., Martins, G. A., Matsueda, H., McKain, K., Meijer, H., Meinhardt, F., Merchant, L., Metzger, J.-M., Mihalopoulos, N., Miles, N. L., Miller, C. E., Mitchell, L., Monteiro, V., Montzka, S., Moossen, H., Moreno, C., Morgan, E., Morgui, J.-A., Morimoto, S., Munger, J. W., Munro, D., Mutuku, M., Myhre, C. L., Mölder, M., Müller-Williams, J., Nakaoka, S.-I., Necki, J., Newman, S., Nichol, S., Nisbet, E., Niwa, Y., Njiru, D. M., Noe, S. M., Nojiri, Y., O'Doherty, S., Obersteiner, F., Paplawsky, B., Parworth, C. L., Peischl, J., Peltola, O., Peters, W., Philippon, C., Piacentino, S., Pichon, J.

M., Pickers, P., Piper, S., Pitt, J., Plass-Dülmer, C., Platt, S. M., Prinzivalli, S., Ramonet, M., Ramos, R., Ren, X., Reyes-Sanchez, E., Richardson, S. J., Rigouleau, L.-J., Riris, H., Rivas, P. P., Rothe, M., Roulet, Y.-A., Ryerson, T., Ryoo, J.-M., Sargent, M., Sasakawa, M., Schaefer, H., Scheeren, B., Schmidt, M., Schuck, T., Schumacher, M., Seibel, J., Seifert, T., Sha, M. K., Shepson, P., Shin, D., Shook, M., Sloop, C. D., Smale, D., Smith, P. D., Spain, G., St. Clair, J. M., Steger, D., Steinbacher, M., Stephens, B., Sweeney, C., Sørensen, L. L., Taipale, R., Takatsuji, S., Tans, P., Thoning, K., Timas, H., Torn, M., Trisolino, P., Turnbull, J., Vermeulen, A., Viner, B., Vitkova, G., Walker, S., Watson, A., Weiss, R., Weyrauch, D., Wofsy, S. C., Worsey, J., Worthy, D., Xueref-Remy, I., Yates, E. L., Young, D., Yver-Kwok, C., Zaehle, S., Zahn, A., Zellweger, C., Zimnoch, M., de Souza, R. A., di Sarra, A. G., van Dinther, D., and van den Bulk, P.: CarbonTracker CT-NRT.v2024-5, NOAA Earth System Research Laboratory [dataset], https://doi.org/10.15138/atpd-k925, 2024.

Mai, J., Yu, L., Deng, T., Wu, D., Qing, P., and Yu, X.: Impact of sea-land breezes on the ozone pollution over the Pearl River Estuary, China Environmental Science, 45(03), 1198-1209, https://doi.org/10.19674/j.cnki.issn1000-6923.20241102.001, 2024.

Mitchell, L. E., Lin, J. C., Bowling, D. R., Pataki, D. E., Strong, C., Schauer, A. J., Bares, R., Bush, S. E., Stephens, B. B., and Mendoza, D.: Long-term urban carbon dioxide observations reveal spatial and temporal dynamics related to urban characteristics and growth, P. Natl. Acad. Sci. Usa., 115, 2912-2917, https://doi.org/10.1073/pnas.1702393115, 2018.

Qiu, X. and Fan, S.: Study on the application of auto-meteorological station data in local circulations analysis such as the sea-land breeze, Acta Scientiarum Naturalium Universitatis Sunyatseni, 52(2), 133-136, https://doi.org/10.13471/j.cnki.acta.snus.2013.02.025, 2013.

Schuldt, K. N., Mund, J., Aalto, T., Abshire, J. B., Aikin, K., Allen, G., Andrade, M., Andrews, A., Apadula, F., Arnold, S., Baier, B., Bakwin, P., Bartyzel, J., Bentz, G., Bergamaschi, P., Beyersdorf, A., Biermann, T., Biraud, S. C., Blanc, P.-E., Boenisch, H., Bowling, D., Brailsford, G., Brand, W. A., Brunner, D., Bui, T. P., Burban, B., Bäni, L., Calzolari, F., Chang, C. S., Chen, H., Chen, G., Chmura, L., Clark, S., Climadat, S., Colomb, A., Commane, R., Condori, L., Conen, F., Conil, S., Couret, C., Cristofanelli, P., Cuevas, E., Curcoll, R., Daube, B., Davis, K. J., De Mazière, M., De Wekker, S., Dean-Day, J. M., Della Coletta, J., Delmotte, M., Di Iorio, T., DiGangi, E., DiGangi, J. P., Dickerson, R., Elsasser, M., Emmenegger, L., Fang, S., Forster, G., France, J., Frumau, A., Fuente-Lastra, M., Galkowski, M., Gatti, L. V., Gehrlein, T., Gerbig, C., Gheusi, F., Gloor, E., Goto, D., Griffis, T., Hammer, S., Hanisco, T. F., Hanson, C., Haszpra, L., Hatakka, J., Heimann, M., Heliasz, M., Heltai, D., Henne, S., Hensen, A., Hermans, C., Hermansen, O., Hintsa, E., Hoheisel, A., Holst, J., Iraci, L. T., Ivakhov, V., Jaffe, D. A., Jordan, A., Joubert, W., Kang, H.-Y., Karion, A., Kawa, S. R., Kazan, V., Keeling, R. F., Keronen, P., Kim, J., Klausen, J., Kneuer, T., Ko, M.-Y., Kolari, P., Kominkova, K., Kort, E., Kozlova, E., Krummel, P. B., Kubistin, D., Kulawik, S. S., Kumps, N., Labuschagne, C., Lam, D. H., Lan, X., Langenfelds, R. L., Lanza, A., Laurent, O., Laurila, T., Lauvaux, T., Lavric, J., Law, B. E., Lee, C.-H., Lee, J., Lehner, I., Lehtinen, K., Leppert, R., Leskinen, A., Leuenberger, M., Leung, W. H., Levin, I., Levula, J., Lin, J., Lindauer, M., Lindroth, A., Loh, Z. M., Lopez, M., Lunder, C. R., Löfvenius, M. O., Machida, T., Mammarella, I., Manca, G., Manning, A., Manning, A., Marek, M. V., Marklund, P., Marrero, J. E., Martin, M. Y., Martin, D., Martins, G. A., Matsueda, H., McKain, K., Meijer, H., Meinhardt, F., Merchant, L., Metzger, J.-M., Mihalopoulos, N., Miles, N. L., Miller, C. E., Miller, J. B., Mitchell, L., Monteiro, V., Montzka, S., Moossen, H., Moreno, C., Morgan, E., Morgui, J.-A., Morimoto, S., Munger, J. W., Munro, D., Mutuku, M., Myhre, C. L., Mölder, M., Müller-Williams, J., Nakaoka, S.-I., Necki, J., Newman, S., Nichol, S., Nisbet, E., Niwa, Y., Njiru, D. M., Noe, S. M., Nojiri, Y., O'Doherty, S., Obersteiner, F., Paplawsky, B., Parworth, C. L., Peischl, J., Peltola, O., Peters, W., Philippon, C., Piacentino, S., Pichon, J. M., Pickers, P., Piper, S., Pitt, J., Plass-Dülmer, C., Platt, S. M., Prinzivalli, S., Ramonet, M., Ramos, R., Ren, X., Reyes-Sanchez, E., Richardson, S. J., Rigouleau, L.-J., Riris, H., Rivas, P. P., Rothe, M., Roulet, Y.-A., Ryerson, T., Ryoo, J.-M., Sargent, M., Sasakawa, M., Schaefer, H., Scheeren, B., Schmidt, M., Schuck, T., Schumacher, M., Seibel, J., Seifert, T., Sha, M. K., Shepson, P., Shin, D., Shook, M., Sloop, C. D., Smale, D., Smith, P. D., Spain, G., St. Clair, J. M., Steger, D., Steinbacher, M., Stephens, B., Sweeney, C., Sørensen, L. L., Taipale, R., Takatsuji, S., Tans, P., Thoning, K., Timas, H., Torn, M., Trisolino, P., Turnbull, J., Vermeulen, A., Viner, B., Vitkova, G., Walker, S., Watson, A., Weiss, R., Weyrauch, D., Wofsy, S. C., Worsey, J., Worthy, D., Xueref-

Remy, I., Yates, E. L., Young, D., Yver-Kwok, C., Zaehle, S., Zahn, A., Zellweger, C., Zimnoch, M., de Souza, R. A., di Sarra, A. G., van Dinther, D., and van den Bulk, P.: Multi-laboratory compilation of atmospheric carbon dioxide data for the period 1957-2023 (obspack_co2_1_test_GLOBALVIEWplus_v10.1_2024-11-13), NOAA Earth System Research Laboratory, Global Monitoring Laboratory [dataset], https://doi.org/10.25925/20241101, 2024.

Thoning, K. W., Tans, P. P., and Komhyr, W. D.: Atmospheric carbon dioxide at Mauna Loa Observatory: 2. Analysis of the NOAA GMCC data, 1974–1985, J. Geophys. Res.-Atmos., 94, 8549-8565, https://doi.org/10.1029/JD094iD06p08549, 1989.

Verhulst, K. R., Karion, A., Kim, J., Salameh, P. K., Keeling, R. F., Newman, S., Miller, J., Sloop, C., Pongetti, T., and Rao, P.: Carbon dioxide and methane measurements from the Los Angeles Megacity Carbon Project–Part 1: calibration, urban enhancements, and uncertainty estimates, Atmos. Chem. Phys., 17, 8313-8341, https://doi.org/10.5194/acp-17-8313-2017, 2017.

Zhang, L., Lin, J., Shao, Y., Huang, S., Fan, S., and Wei, W.: Understanding the impact of sea and land breezes on ozone pollution in the Pearl River Delta, Acta Scientiae Circumstantiae, 44(1), 74-85, https://doi.org/10.13671/j.hjkxxb.2023.0285, 2024.